Geophysical Research Letters

RESEARCH LETTER
10.1029/2020GL087363

Key Points:
- Phase transition of $MgSiO_3$-$FeSiO_3$ solid solutions was investigated to 24.3 GPa and 800 K using single-crystal X-ray diffraction
- Metastable orthopyroxene progressively transforms into the β-opx and γ-opx phase at high temperature (800 K) and high pressure
- Metastable orthopyroxene and its high-pressure phases could exist within the coldest part of old slabs and contribute to slab stagnation

Supporting Information:
- Supporting Information S1

Correspondence to:
D. Fan,
fandawei@vip.gyig.ac.cn

Citation:
Xu, J., Fan, D., Zhang, D., Guo, X., Zhou, W., & Dera, P. K. (2020). Phase transition of enstatite-ferrosilite solid solutions at high pressure and high temperature: Constraints on metastable orthopyroxene in cold subduction. *Geophysical Research Letters*, *47*, e2020GL087363. https://doi.org/10.1029/2020GL087363

Received 2 FEB 2020
Accepted 20 APR 2020
Accepted article online 12 MAY 2020

Phase Transition of Enstatite-Ferrosilite Solid Solutions at High Pressure and High Temperature: Constraints on Metastable Orthopyroxene in Cold Subduction

Jingui Xu[1,2], Dawei Fan[1], Dongzhou Zhang[2], Xinzhuan Guo[1], Wenge Zhou[1], and Przemyslaw K. Dera[2]

[1]Key Laboratory for High-Temperature and High-Pressure Study of the Earth's Interior, Institute of Geochemistry, Chinese Academy of Sciences, Guiyang, China, [2]Hawai'i Institute of Geophysics and Planetology, School of Ocean and Earth Science and Technology, University of Hawai'i at Manoa, Honolulu, HI, USA

Abstract $(Mg, Fe)SiO_3$ orthopyroxene is an abundant mineral of oceanic subducting slabs. In-situ high-pressure and high-temperature single-crystal X-ray diffraction has been used to investigate the phase transition of orthopyroxene across the enstatite-ferrosilite (En-Fs) join ($En_{70}Fs_{30}$, $En_{55}Fs_{45}$, $En_{44}Fs_{56}$ and Fs_{100}) up to 24.3 GPa and 800 K, simulating conditions within the coldest part of a subduction zone consisting of an old and rapidly subducting slab. Instead of the orthopyroxene → high-pressure clinopyroxene transition, the α-opx → β-opx and β-opx → γ-opx phase transition are observed at 7.2–15.3 and 11.6–21.1 GPa (depending on the Fs content), respectively. This study indicates that the pressure-induced phase transition of $(Mg, Fe)SiO_3$ orthopyroxene under relatively low temperature (<800 K) could be different than those occurring under relatively high temperature (>800 K). Additionally, the α-opx → β-opx → γ-opx phase transition could exist within the center of the extremely cold slabs (like Tonga), where such low temperature persists to ~600-km depth.

Plain Language Summary $(Mg, Fe)SiO_3$ is the most abundant chemical compound in Earth's mantle. Investigating its phase relations at high-pressure and high-temperature is of fundamental importance in constraining the composition and understanding the structure of the Earth's interior. Previous studies have well established the phase diagram of $(Mg, Fe)SiO_3$ at high pressure and high temperature. Orthopyroxene is a low-pressure phase; with increasing pressure and temperature, orthopyroxene transforms to the high-pressure clinopyroxene, then, it transforms to akimotoite or decomposes to wadsleyite + stishovite. These phase transitions require temperatures higher than 900 K, which are easily satisfied in the normal mantle or relatively warm subduction zone conditions. However, extremely low-temperature region exists in the center of some old and rapidly subducting slabs (e.g., Tonga), and such low-temperature region (~800 K) can extend to ~600-km depth. In this study, we investigate the phase relations of $(Mg, Fe)SiO_3$ orthopyroxene with several different compositions to 24.3 GPa and 800 K. A different phase transition path is observed, that is, the α-opx → β-opx → γ-opx at pressures within the transition zone depths. Therefore, the result of this study adds one more piece of information to our understanding of phase relations of $(Mg, Fe)SiO_3$ orthopyroxene within the extremely cold subducted slabs.

1. Introduction

Orthopyroxene is a major component of the Earth's crust and upper mantle. Thus, understanding its equation of state (EoS) and phase transition at high pressure and high temperature is very important for constraining the composition and structure of these regions (e.g., Frost, 2008). Ultramafic rocks were transported as xenoliths to the Earth's surface and are direct samples of the upper mantle; peridotite (harzburgite and lherzolite) and pyroxenite (websterite) have orthopyroxene as one of their major mineral constituents. For instance, the orthopyroxene content of mantle harzburgite and lherzolite can be as high as 40% (Bodinier & Godard, 2007), and the orthopyroxene content of websterite is generally higher than that of peridotite and can be as high as 60% (e.g., Xu et al., 2013).

Enstatite (En_{100}, $MgSiO_3$) and ferrosilite (Fs_{100}, $FeSiO_3$) are two important endmembers of mantle orthopyroxene, and the composition of orthopyroxene $(Mg_x, Fe_{1-x})SiO_3$ varies in different rock types. Mineral inclusions in diamond provide key information on the chemical composition and mineral assemblages of mantle

rocks. Statistics on diamond inclusions (Stachel & Harris, 2008) indicated that peridotitic orthopyroxene has an average Mg# (100 Mg/(Mg + Fe)) of 94, while its minimum and maximum Mg# are 81 and 97, respectively. In comparison, websteritic orthopyroxene is much richer in Fe than peridotitic orthopyroxene, and the average, minimum, and maximum Mg# are 84, 76, and 93, respectively. Some orthopyroxene inclusions in diamond have very high-Fe contents, with Mg# as low as 57, and have been identified as the result of the retrograde transformation of bridgmanite (Walter et al., 2011). Orthopyroxene with Fs contents greater than 50 (mol.%) to content amounts near that of the Fs_{100} endmember is also present in high-pressure metamorphic rocks (e.g., Brothers & Yokoyama, 1990; Davidson, 1968; Jaffe et al., 1978). Therefore, it is necessary to investigate the effects of the variation in Fe on the phase transition of orthopyroxene for modeling orthopyroxene in the deep crust and upper mantle.

The structure of orthopyroxene under ambient conditions has been described in great detail (e.g., Cameron & Papike, 1981) and is orthorhombic with *Pbca* symmetry. The phase transition of orthopyroxene at high pressure is largely dependent on temperature. Along the normal mantle geotherm in a pyrolite mineralogy model, orthopyroxene undergoes a phase transition at ~8 GPa; the transition is from an initial orthorhombic *Pbca* symmetry to a monoclinic *C*2/*c* symmetry (high-pressure clinopyroxene; e.g., Shinmei et al., 1999; Akashi et al., 2009), and finally, it is absorbed into majoritic garnet (Frost, 2008). On the other hand, investigating the metastable phase transition of orthopyroxene at high pressure and relatively low temperature has important geophysical implications; low-temperature zones exist in Earth's subduction zones, allowing slab minerals to be preserved as a metastable phase at greater depths than those under equilibrium conditions (e.g., Faccenda & Dal Zilio, 2017; Kirby et al., 1991; Kirby et al., 1996; Van Mierlo et al., 2013). To date, several metastable phase transitions of orthopyroxene have been identified by various experimental methods, including X-ray diffraction (XRD; e.g., Hugh-Jones et al., 1996; Zhang et al., 2012; Dera et al., 2013; Zhang et al., 2013; Li et al., 2014; Finkelstein et al., 2015; Xu et al., 2018), ultrasonic measurements (Kung et al., 2004), Raman spectroscopy (Lin, 2004; Serghiou et al., 2000; Zhang et al., 2013; Zhang et al., 2014), Brillouin spectroscopy (Zhang & Bass, 2016), Mössbauer spectroscopy (Zhang et al., 2011), and nuclear resonant inelastic X-ray scattering spectroscopy (Zhang, Jackson, et al., 2013).

One conclusion from previous studies is that the metastable phase transition of orthopyroxene is compositionally dependent. En_{100} transforms from its initial orthorhombic *Pbca* symmetry (α-opx) to β-opx ($P2_1/c$) at ~12 GPa (Kung et al., 2004; Lin, 2004; Xu et al., 2018), which survives to ~40 GPa until it undergoes a phase transition accompanied by a IV-to-VI coordination change of Si (Serghiou et al., 2000). Natural $En_{90}Fs_{10}$ orthopyroxene undergoes two further phase transitions (at 29.9 and 40.3 GPa) after the α-opx → β-opx transition (14.6 GPa), which are named α-popx and β-popx, and both α-popx and β-popx have $Pca2_1$ symmetry (Finkelstein et al., 2015). Natural Fe-rich $En_{18}Fs_{82}$ orthopyroxene undergoes the α-opx → β-opx transition at 11.1 GPa; however, this transition is followed by a different high-pressure phase at 13.0 GPa, named γ-opx, which has *Pbca* symmetry (Dera, Finkelstein, et al., 2013). Fs_{100} orthopyroxene is very different from the above-mentioned orthopyroxenes and transforms into a monoclinic phase with *C*2/*c* symmetry at ~4.2 GPa (Hugh-Jones et al., 1996). Therefore, the phase transitions of orthopyroxene across the En-Fs solid solution cannot be well constrained until investigating orthopyroxenes with intermediate compositions between $En_{90}Fs_{10}$ and $En_{18}Fs_{82}$.

Most of the previous studies were carried out at room temperature; however, geophysical modeling suggested the lowest temperature at the coldest part of the famous cold subducting slab in Tonga is ~800 K at ~600-km depth (e.g., Bina & Navrotsky, 2000; Ganguly et al., 2009; King et al., 2015). Existing high-pressure and high-temperature studies on the metastable phase transition of orthopyroxene cannot prove the existence of these identified room-temperature high-pressure metastable phases (e.g., β- and γ-opx) in deep subduction zones, even in a cold subduction zone, either because of the limited experimental pressure range or because of the limited compositional range of sample (de Vries et al., 2013; Xu et al., 2018; Zhang et al., 2014; Zhao et al., 1995).

A large number of studies have measured the EoS of orthopyroxene with different compositions utilizing XRD combined with diamond anvil cells (DACs). These studies have provided good constraints on the EoS of En_{100} and Fs_{100} (e.g., Angel & Hugh-Jones, 1994; Zhao et al., 1995; Hugh-Jones & Angel, 1997; Angel & Jackson, 2002; Periotto et al., 2012; Xu et al., 2018); additionally, numerous studies have been carried out on orthopyroxene with intermediate compositions, including natural (e.g., Hugh-Jones &

Angel, 1997; Nestola et al., 2008; Dera, Finkelstein, et al., 2013; Xu et al., 2016) and synthetic samples (e.g., Hugh-Jones & Angel, 1997; Zhang, Jackson, et al., 2013). On the other hand, the thermal expansion properties of synthetic orthopyroxene along the En-Fs join have been investigated (Hugh-Jones, 1997; Sueno et al., 1976; Yang & Ghose, 1994); however, thermal EoS studies in terms of measuring volume at simultaneously high pressure and high temperature are still limited to endmember orthopyroxenes (de Vries et al., 2013; Xu et al., 2018; Zhao et al., 1995).

In this study, we synthesized orthopyroxene with four different compositions along the En-Fs join ($En_{70}Fs_{30}$, $En_{55}Fs_{45}$, $En_{44}Fs_{56}$, and Fs_{100}) and investigated them with high-pressure single-crystal XRD (SCXRD) using DAC. Furthermore, SCXRD data were also collected at simultaneously high pressure and high temperature on $En_{70}Fs_{30}$, $En_{44}Fs_{56}$, and Fs_{100} to 24.3 GPa and 800 K, and the collected pressure-volume-temperature (*P-V-T*) data were used to derive the thermal EoS. This work aims to constrain the metastable phase transition and thermal EoS of orthopyroxene along the En-Fs join under conditions within the coldest part of a subduction zone consisting of an old slab.

2. Methods

We synthesized four orthopyroxenes with compositions along the En-Fs join, including $En_{70}Fs_{30}$, $En_{55}Fs_{45}$, $En_{44}Fs_{56}$, and Fs_{100} (supporting information Figures S1–S2 and Table S1). SCXRD experiments (Figures S3–S6) were carried out at the13-BM-C experimental station of the Advanced Photon Source, Argonne National Laboratory. Data were analyzed by GSE_ADA/RSV (Dera et al., 2013), APEX3 Crystallography Software Suite, and SHELXL package (Sheldrick, 2008). The details of sample synthesis, SCXRD experiments, and data processing are provided in Text S1 (Balan et al., 2013; Bell et al., 1995; Dera, Zhuravlev, et al., 2013; Dolomanov et al., 2009; Fan et al., 2017; Fei et al., 2007; Koch-Müller et al., 2004; Momma & Izumi, 2011; Rauch & Keppler, 2002; Rivers et al., 2008; Sheldrick, 2008; Stalder et al., 2015; Xu et al., 2017; Xu et al., 2018; Xu et al., 2019; Zhang et al., 2017).

3. Results and Discussion

3.1. Phase Transition of En-Fs Orthopyroxene at High Pressure and Room Temperature

The ambient SCXRD results firmly confirmed that $En_{70}Fs_{30}$, $En_{55}Fs_{45}$, $En_{44}Fs_{56}$, and Fs_{100} were successfully synthesized. However, the incorporation of several hundred ppm water results in a weak positive volume in the mixing properties of En-Fs solid solutions (Text S2 and Figure S7; Domeneghetti & Steffen, 1992; Hugh-Jones et al., 1997; Tarantino et al., 2002; Ohi & Miyake, 2016; Ye, 2016; Xu et al., 2018). Analyses of the high-pressure and room-temperature SCXRD data of $En_{70}Fs_{30}$, $En_{55}Fs_{45}$, $En_{44}Fs_{56}$, and Fs_{100} indicated that all orthopyroxenes exhibited similar behaviors of phase transition, which resembled the phase transition path of $En_{18}Fs_{82}$ from a previous study (Dera, Finkelstein, et al., 2013), although they contained several hundred ppm water. As shown in Figure S5, these orthopyroxenes underwent two phase transitions characterized by significant changes observed in the SCXRD image. The SCXRD images of the first high-pressure phase have more peaks than the initial α-opx phase, while the number of peaks is shown to significantly decrease after the second phase transition. The diffraction peaks of the initial orthopyroxene phase of the four compositions were well indexed using the orthorhombic *Pbca* α-opx unit cell (Tables S2–S3). Indexing and symmetry analyses of the first high-pressure phase resulted in a similar monoclinic phase (Table S2) as the β-opx phase ($P2_1/c$) reported by previous studies (Dera, Finkelstein, et al., 2013; Finkelstein et al., 2015; Xu et al., 2018; Zhang et al., 2012). The structures were refined only for $En_{70}Fs_{30}$ and $En_{44}Fs_{56}$ (Table S4) due to the limited effective diffraction peaks caused by the partial overlap of peaks from two twinning domains (Dera, Finkelstein, et al., 2013; Finkelstein et al., 2015; Xu et al., 2018). The second high-pressure phase occurs with a higher crystal symmetry, as indicated by the disappearance of the twinning domains introduced by the first transition. Again, the four orthopyroxenes share the same symmetry as that of the *Pbca* space group. Similarly, the second high-pressure phase is the same as the γ-opx phase reported by the previous study on $En_{18}Fs_{82}$ since the structure has been successfully refined on the four orthopyroxenes in this study using the γ-opx phase as an initial model (Table S5). The features of the α-opx → β-opx and β-opx → γ-opx phase transitions are predominantly characterized by a tetrahedral rotation (Dera, Finkelstein, et al., 2013; Finkelstein et al., 2015; Xu et al., 2018; Zhang et al., 2012).

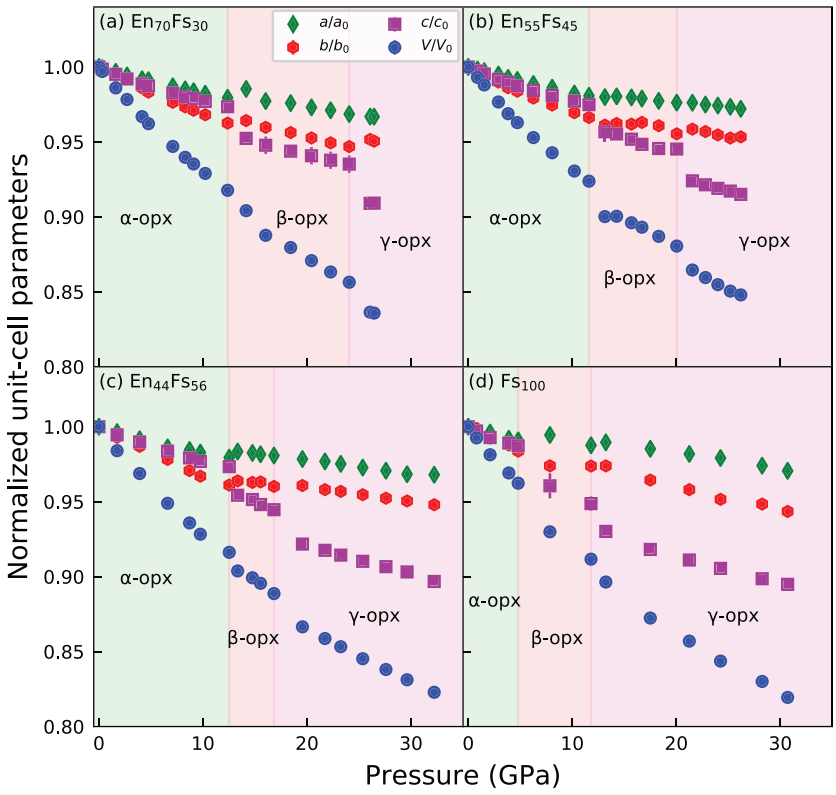

Figure 1. (a–d)Unit-cell parameters a, b, c, and volume V of $En_{70}Fs_{30}$, $En_{55}Fs_{45}$, $En_{44}Fs_{56}$, and Fs_{100} as a function of pressure, across the α-opx → β-opx and β-opx → γ-opx phase transitions.

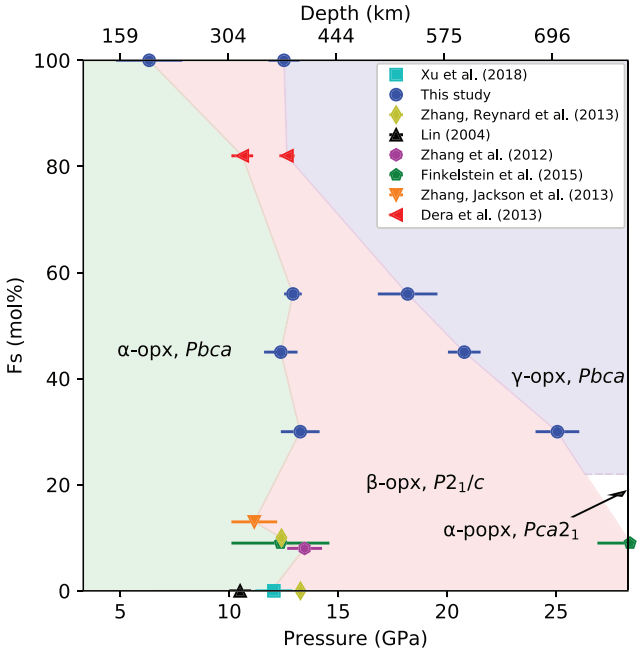

Figure 2. Metastable phase boundary of orthopyroxene across the En-Fs join at room temperature and high pressure. The data included are from this study and previous studies (Dera, Finkelstein, et al., 2013; Finkelstein et al., 2015; Lin, 2004; Xu et al., 2018; Zhang et al., 2012; Zhang, Jackson, et al., 2013; Zhang, Reynard, et al., 2013). The PREM model (Dziewonski & Anderson, 1981) is used to convert pressure to depth.

The unit-cell parameters of the orthopyroxenes as a function of pressure are shown in Figures 1 and S8, which characterize the α-opx → β-opx and β-opx → γ-opx phase transition as a first-order phase transition. The evolution of the monoclinic angle through the phase transition indicates that the symmetry varies from orthorhombic in the initial α-opx phase to monoclinic in the β-opx, and orthorhombic symmetry appears again in the γ-opx (Figure S8). As shown in Figure 1, the volume drops are 1.5–3.4% and 1.7–2.5% for the α-opx → β-opx and β-opx → γ-opx transitions, respectively. The a- and b-axes show different behaviors among the four orthopyroxenes. In the first transition, the a-axis of $En_{70}Fs_{30}$, $En_{44}Fs_{56}$, and Fs_{100} expands more obviously (0.4–0.6%) than that of $En_{55}Fs_{45}$, which shows that the a-axis behaves continuously. In the second phase transition, the a-axis of the only Fs_{100} expands by 0.2%, while those of the other orthopyroxenes show continuous decompressions. The b-axis of $En_{70}Fs_{30}$ and $En_{44}Fs_{56}$ expands by 0.4–0.6% in the α-opx → β-opx transition, while those of $En_{55}Fs_{45}$ and Fs_{100} decrease by 0.1–1%. In the β-opx → γ-opx transition, the b-axes of $En_{70}Fs_{30}$, $En_{55}Fs_{45}$, and $En_{44}Fs_{56}$ expand by 0.1–0.5%, which are significantly larger than that of Fs_{100}. The behavior of the c-axis of the four orthopyroxenes are very consistent and continuously decrease by 1.9–2.7% and 2.0–2.8% across the α-opx → β-opx and β-opx → γ-opx phase transitions, respectively.

This study, combined with previous studies, leads to a better constraint on the metastable phase relations of orthopyroxene across

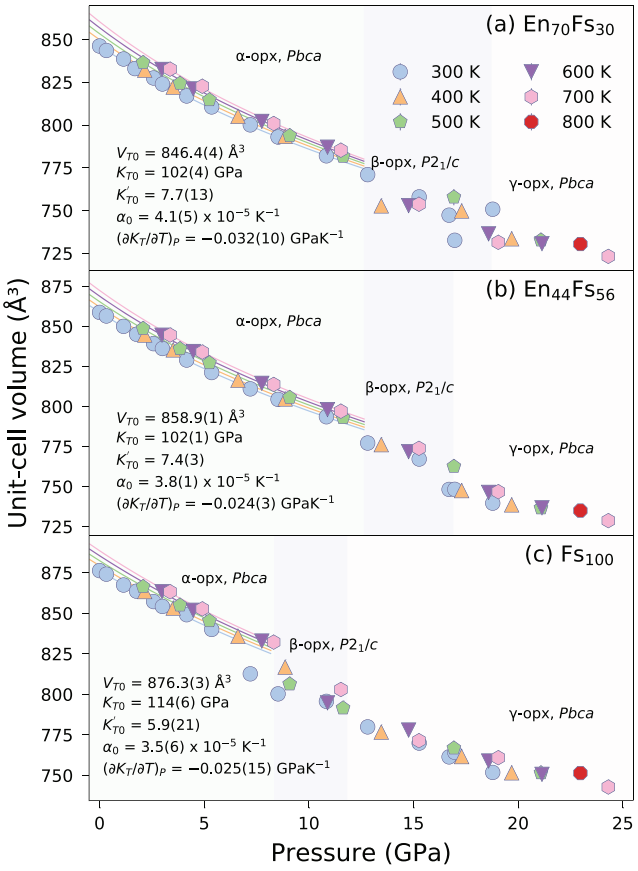

Figure 3. (a–c)The unit-cell volume of $En_{70}Fs_{30}$, $En_{70}Fs_{30}$, and Fs_{100} as a function of pressure and temperature. The obtained thermal EoS parameters (V_{T0}, K_{T0}, K'_{T0}, α_0, and $(\partial K_T/\partial_T)_P$) of the α-opx phase are also shown. The solid curves represent isothermal compression curves at various temperatures which are calculated by using the obtained thermal EoS parameters.

the En-Fs join (Figure 2). As shown in Figure 2, upon compression, α-opx transforms to the β-opx in orthopyroxene with any composition along the En-Fs join. Considering that the incorporation of several hundred ppm water could have insignificant effects on the phase transition pressure of enstatite (Xu et al., 2018), the discussion does not consider the effects of water on shifting the transition pressure. The increasing Fe content results in a decreasing pressure of the α-β transition, while the effects are weaker within the low-Fs range (Fs < 56%) than within the high-Fs range. As shown in Figure 2, within the low-Fs range, the transition pressures are between 11(1) and 13(1) GPa, while Fs_{82} and Fs_{100} have lower transition pressures of 10.6(5) and 6(2) GPa, respectively. By comparison, the effects of increasing the Fe content are more evident for the β-opx → γ-opx transition. Within the low-Fs region, from lowest to highest, the transition pressure decreases from 28(2) to 18(1) GPa, while Fs_{82} and Fs_{100} have approximately identical transition pressures of 12.6(4) and 12.5(7) GPa, respectively. Beyond shifting the transition pressure, increasing the Fe content also affects the structure of the second high-pressure phase. En_{100} does not have a second high-pressure phase transition characterized by a tetrahedral rotation (Xu et al., 2018). The incorporation of Fe leads to the appearance of the α-popx or γ-opx phase (Figure 2); the existing experimental results suggest that the onset of the Fs content during the presence of the α-popx is between 0% and 10%, and that the boundary between the α-popx and γ-opx phase is within Fs = 10–30%.

3.2. Phase Transition of En-Fs Orthopyroxene at High Pressure and High Temperature

Analyses of the high-pressure and high-temperature SCXRD data of $En_{70}Fs_{30}$, $En_{44}Fs_{56}$, and Fs_{100} indicated that their phase transitions are the same as what occurs under room temperature and high pressure (Figures S6 and S9). Refining the crystal structures at high pressure and high temperature was not possible due to the limited opening angle of the externally heated DAC (±16°); however, the obtained unit-cell parameters and analyses of space group confirmed the α-opx → β-opx and β-opx → γ-opx phase transition for $En_{70}Fs_{30}$, $En_{44}Fs_{56}$, and Fs_{100} at high pressure and high temperature (≤800 K). As shown in Figure 3 and Table S6, which indicates that these metastable high-pressure phases of En-Fs orthopyroxene could exist under relatively low temperature (800 K), as suggested by the previous studies on low-Fe orthopyroxenes (Xu et al., 2018; Zhang et al., 2014).

3.3. EoS of the En-Fs Orthopyroxene

The *P-V* data of the four orthopyroxenes within the α-opx phase region were fitted to the third-order Birch-Murnaghan-EoS (BM3-EoS; Birch, 1947) to obtain the EoS parameters including the zero-pressure volume (V_{T0}), isothermal bulk modulus (K_{T0}), and its pressure derivative (K'_{T0}). We compared the results of this study to those results of previous studies, and we found that the effects of the Fs content on the EoS parameters are nonlinear for the hydrous orthopyroxenes, while they are linear for the anhydrous orthopyroxenes (Figure S10 and Table S7; Text S3; Weidner et al., 1978; Bass & Weidner, 1984; Hugh-Jones & Angel, 1994; Flesch et al., 1998; Jackson et al., 1999; Angel, 2000; Jackson et al., 2007; Angel et al., 2014).

The *P-V-T* data of the α-opx phase for $En_{70}Fs_{30}$, $En_{44}Fs_{56}$, and Fs_{100} were used to derive the thermal EoS parameters by fitting the data to the high-temperature BM3-EoS (Text S4). The obtained thermal EoS parameters including the V_{T0}, K_{T0}, K'_{T0}, thermal expansion at room pressure (α_T), and the temperature derivative of K_{T0} at room pressure $(\partial K_T/\partial_T)_P$ are summarized in Table S8 and Figure 3. $En_{70}Fs_{30}$, $En_{44}Fs_{56}$, and Fs_{100} have comparable values on $(\partial K_T/\partial_T)_P$ (−0.024(3) – −0.032(10) GPa/K) and α_T (α_0 = 3.5(6)–4.1(5) $\times 10^{-5}$ K^{-1}). In addition, the thermal expansion coefficients of $En_{70}Fs_{30}$, $En_{44}Fs_{56}$, and Fs_{100} are larger than those of anhydrous orthopyroxenes (Figure S10; Sarver & Hummel, 1962;

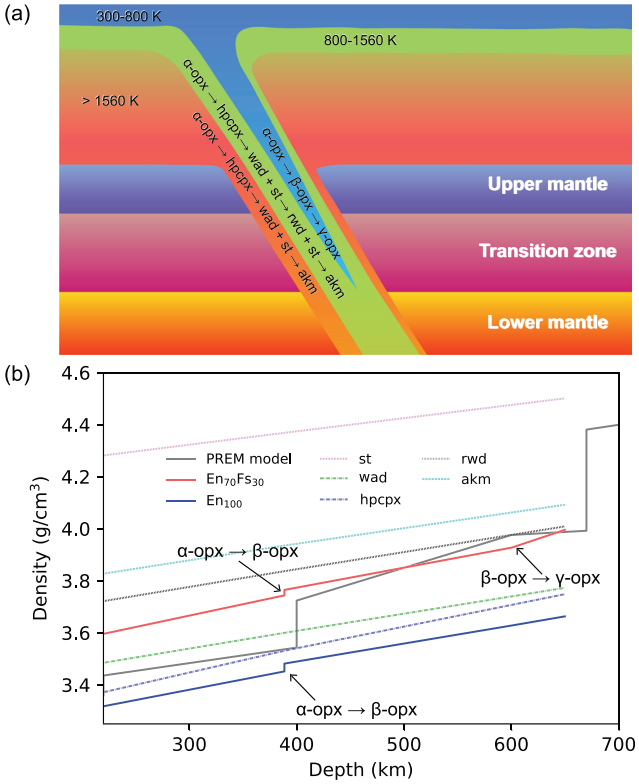

Figure 4. (a) A schematic diagram of a cold subducting slab and the phase relations of (Mg, Fe)SiO_3 orthopyroxene. The temperature distribution is drawn after Ganguly et al. (2009). The phase transition of orthopyroxene at high-temperature regions (>800 K) is from previous studies (e.g., Fei et al., 1990), while the phase transition at low temperature (<800 K) is from this study. The figure is not drawn to scale. Note that pyroxene component would disappear due to the pyroxene-garnet transition in the multiple components rock such as peridotite, which would be inhibited at temperatures <1,673 K in the geological timescales (e.g., Nishi et al., 2013; Van Mierlo et al., 2013) and is not included in this figure. Hpcpx: high-pressure clinopyroxene (*C*2/*c*); wad: wadsleyite; rwd: ringwoodite; akm: akimotoite; st: stishovite. (b) Calculated density profiles of En_{100} and $En_{70}Fs_{30}$ orthopyroxene along 800 K adiabat and comparison with the preliminary reference Earth model (PREM; Dziewonski & Anderson, 1981). The density profiles of other minerals along 1,500 K (hpcpx-$MgSiO_3$, wad-Mg_2SiO_4, rwd-$Mg_{1.8}Fe_{0.2}SiO_4$, akm-$MgSiO_3$ and st-SiO_2) are also shown for comparison.

Skinner, 1966; Frisillo & Barsch, 1972; Dietrich & Arndt, 1982; Jackson et al., 2003), which indicates that the incorporation of water enhances the thermal expansion of orthopyroxene, being consistent with previous studies of En_{100} and other nominally anhydrous silicates (Fan et al., 2017; Xu et al., 2018; Ye, 2016). The thermal EoS parameters of the β- and γ -opx phases were not successfully obtained due to the narrow data coverage (Figure 3).

4. Geophysical Implications

The experimental results in this study have potential implications for the phase relations of (Mg, Fe)SiO_3 orthopyroxene within cold subducting slabs. It is well known that low temperature in subduction zones enables the preservation of metastable phases in the subducting slabs (e.g., Faccenda & Dal Zilio, 2017; Van Mierlo et al., 2013). Alternatively, the phase transition path within a downgoing slab depends on the thermal structure of the slab, and the phase transition of a mineral could be different in different temperature regions. The phase relations of orthopyroxene at high pressure and high temperature (the high-temperature region of a cold subducting slab) have been investigated by several authors (e.g., Akashi et al., 2009; Fei et al., 1990; Ito & Navrotsky, 1985; Ono et al., 2018). As shown in Figure 4a, the orthopyroxene→high-pressure clinopyroxene transition occurs before the decomposition to wadsleyite plus stishovite. Previous experimental studies suggested that the orthopyroxene → high-pressure clinopyroxene transition occurs at temperatures around 1,000 K (Akashi et al., 2009; Woodland, 1998) and the high-pressure clinopyroxene → wadsleyite + stishovite reaction occurs at $T > 1{,}000$ K (e.g., Hogrefe et al., 1994; Ono et al., 2018). However, the phase transition of orthopyroxene in the coldest part of a subducting slab could be different.

The thermal structure of a slab is controlled by several parameters (e.g., age and slab dip), and extremely low-temperature conditions exist within some old and rapidly subducting slabs (Syracuse et al., 2010). For instance, the temperature of the slab center for the Tonga slab was calculated as ~800 K at ~600-km depth (e.g., Bina & Navrotsky, 2000; Ganguly et al., 2009; King et al., 2015). Recent studies suggested that the phase transition of orthopyroxene under such low temperature could be different than that occurs under temperatures higher than 800 K. Zhang et al. (2014) investigated the phase transition of natural orthopyroxene (En_{100} and $En_{90}Fs_{10}$) up to 673 K and 18.2 GPa using in-situ high-pressure and high-temperature Raman spectroscopy. Utilizing high-pressure and high-temperature SCXRD, Xu et al. (2018) investigated the phase transition of synthetic En_{100} up to 23.8 GPa and 600 K. These two studies observed the α-opx to β-opx phase transition instead of the orthopyroxene → high-pressure clinopyroxene transition. In this study, we enlarged the experimental pressure-temperature scope (24.3 GPa and 800 K) and compositional range to investigate the metastable phase transition of (Mg, Fe)SiO_3 orthopyroxene. Similarly, we did not observe the orthopyroxene → high-pressure clinopyroxene transition, the decomposition to wadsleyite + stishovite, or the polymorphic pyroxene-akimotoite transition, instead, the α-opx → β-opx → γ-opx phase transition was observed (Figure 4a). Therefore, this study indicates that, in the coldest part of an old and rapidly subducting slab (like Tonga), the phase transition path of (Mg, Fe)SiO_3 orthopyroxene could be the α-opx → β-opx → γ-opx, which is different than those occurring in the higher temperature region (Figure 4a).

We calculated the density-depth profile of En_{100} and $En_{70}Fs_{30}$ along 800 K and to 650 km, and the results were compared with the preliminary reference Earth model (PREM; Dziewonski & Anderson, 1981). The

high-temperature BM3-EoS was used for the calculation. The thermal EoS parameters of En_{100} were adopted from Xu et al. (2018). The thermal EoS parameters of the α-opx phase of $En_{70}Fs_{30}$ were from this study, while the thermal EoS parameters of the β-opx of En_{100} were used for the β-opx phase of $En_{70}Fs_{30}$. The density of the γ-opx phase of $En_{70}Fs_{30}$ was not calculated using the thermal EoS as no thermal EoS has been available, instead, it was calculated from the measured unit-cell volume at 22.98 GPa and 800 K. Furthermore, we calculated the density profiles along 1,500 K for other high-pressure polymorphs (high-pressure clinopyroxene and akimotoite) and the decomposition products (wadsleyite, ringwoodite, and stishovite) of orthopyroxene. The used thermal EoS parameters are shown in Table S9 (Katsura et al., 2009; Liu et al., 1999; Nishihara et al., 2004; Shinmei et al., 1999; Wang et al., 2004). As shown in Figure 4b, the density of $En_{70}Fs_{30}$ is higher than that of En_{100} within the whole depth range, indicating the enrichment of Fe in orthopyroxene enhances the slab subduction in the upper mantle. During the α-opx → β-opx transition (~390 km) the density jumps are less than 1%, which are much lower than the density jump (~5%) of the PREM at ~410 km. The density of the γ-opx phase of $En_{70}Fs_{30}$ is comparable to the density of the PREM at 650 km, as the Fe content of $En_{70}Fs_{30}$ is significantly higher than those of normal mantle orthopyroxenes. In the transition zone, the density of $En_{70}Fs_{30}$ is higher than those of wadsleyite and high-pressure clinopyroxene due to the higher Fe content; however, the density of En_{100} is the lowest among these minerals. The results indicate that the metastable orthopyroxene has the lowest density compared to other high-pressure polymorphs in the transition zone when the Fe contents are comparable. Therefore, the existence of metastable (Mg, Fe)SiO_3 orthopyroxene within the coldest part of a cold subducting slab would decrease the negative buoyancy of a slab and thus contribute to the slab stagnation in the transition zone.

Acknowledgments

We would like to acknowledge Sergey N. Tkachev for help with gas loading. This project was funded by the National Natural Science Foundation of China (41772043 and 41802043), the Chinese Academy of Sciences "Light of West China" Program (2017, 2019), the Youth Innovation Promotion Association CAS (Dawei Fan, 2018434), and Innovation and Entrepreneurship Funding of High-Level Overseas Talents of Guizhou Province (Dawei Fan, [2019]10). Part of this work was supported by the National Science Foundation of the United States (EAR-1722969). The experiments were performed at GeoSoilEnviroCARS (Sector 13), Partnership for Extreme Crystallography program (PX^2), Advanced Photon Source (APS), and Argonne National Laboratory. GeoSoilEnviroCARS is supported by the National Science Foundation—Earth Sciences (EAR-1634415) and the Department of Energy—Geosciences (DE-FG02-94ER14466). PX^2 program is supported by COMPRES under NSF Cooperative Agreement EAR-1661511. The use of the COMPRES-GSECARS gas loading system was supported by COMPRES under NSF Cooperative Agreement EAR-1661511 and by GSECARS. Use of the Advanced Photon Source was supported by the U. S. Department of Energy, Office of Science, Office of Basic Energy Sciences, under Contract No. DE-AC02-06CH11357. We would like to thank two anonymous reviewers for their thorough and insightful comments and Steve Jacobsen for handling this paper. Per AGU's Data Policy, the supporting data have been deposited in a general repository, Zenodo, http://doi.org/10.5281/zenodo.3810931.

References

Akashi, A., Nishihara, Y., Takahashi, E., Nakajima, Y., Tange, Y., & Funakoshi, K.i. (2009). Orthoenstatite/clinoenstatite phase transformation in $MgSiO_3$ at high-pressure and high-temperature determined by in situ X-ray diffraction: Implications for nature of the X discontinuity. *Journal of Geophysical Research*, *114*, B04206. https://doi.org/10.1029/2008JB005894

Angel, R., & Hugh-Jones, D. (1994). Equations of state and thermodynamic properties of enstatite pyroxenes. *Journal of Geophysical Research: Solid Earth (1978–2012)*, *99*(B10), 19777–19783. https://doi.org/10.1029/94JB01750

Angel, R. J. (2000). Equations of state. *Reviews in Mineralogy and Geochemistry*, *41*(1), 35–59. https://doi.org/10.2138/rmg.2000.41.2

Angel, R. J., Gonzalez-Platas, J., & Alvaro, M. (2014). EosFit7c and a Fortran module (library) for equation of state calculations. *Zeitschrift Fur Kristallographie*, *229*(5), 405–419. https://doi.org/10.1515/zkri-2013-1711

Angel, R. J., & Jackson, J. M. (2002). Elasticity and equation of state of orthoenstatite, $MgSiO_3$. *American Mineralogist*, *87*(4), 558–561. https://doi.org/10.2138/am-2002-0419

Balan, E., Blanchard, M., Yi, H., & Ingrin, J. (2013). Theoretical study of OH-defects in pure enstatite. *Physics and Chemistry of Minerals*, *40*(1), 41–50. https://doi.org/10.1007/s00269-012-0544-6

Bass, J. D., & Weidner, D. J. (1984). Elasticity of single-crystal orthoferrosilite. *Journal of Geophysical Research: Solid Earth*, *89*(B6), 4359–4371. https://doi.org/10.1029/JB089iB06p04359

Bell, D. R., Ihinger, P. D., & Rossman, G. R. (1995). Quantitative-analysis of trace OH in garnet and pyroxenes. *American Mineralogist*, *80*(5–6), 465–474. https://doi.org/10.2138/am-1995-5-607

Bina, C. R., & Navrotsky, A. (2000). Possible presence of high-pressure ice in cold subducting slabs. *Nature*, *408*(6814), 844–847. https://doi.org/10.1038/35048555

Birch, F. (1947). Finite elastic strain of cubic crystals. *Physical Review*, *71*(11), 809–824. https://doi.org/10.1103/PhysRev.71.809

Bodinier, J.L., & Godard, M. (2007) Orogenic, ophiolitic, and abyssal peridotites. In H.D. Holland, and K.K. Turekian, Eds. *Treatise on geochemistry*, 2, p. 1–73. Pergamon, Oxford. https://doi.org/10.1016/B0-08-043751-6/02004-1

Brothers, R. N., & Yokoyama, K. (1990). Fe-rich pyroxenes from a microdiorite dike, Whangarei, New Zealand. *American Mineralogist*, *75*(5–6), 620–630.

Cameron, M., & Papike, J. (1981). Structural and chemical variations in pyroxenes. *American Mineralogist*, *66*(1–2), 1–50.

Davidson, L. (1968). Variation in ferrous iron-magnesium distribution coefficients of metamorphic pyroxenes from Quairading, Western Australia. *Contributions to Mineralogy and Petrology*, *19*(3), 239–259. https://doi.org/10.1007/BF00508913

de Vries, J., Jacobs, M., van den Berg, A., Wehber, M., Lathe, C., McCammon, C., et al. (2013). Thermal equation of state of synthetic orthoferrosilite at lunar pressures and temperatures. *Physics and Chemistry of Minerals*, *40*(9), 691–703. https://doi.org/10.1007/s00269-013-0605-5

Dera, P., Finkelstein, G. J., Duffy, T. S., Downs, R. T., Meng, Y., Prakapenka, V., & Tkachev, S. (2013). Metastable high-pressure transformations of orthoferrosilite Fs_{82}. *Physics of the Earth and Planetary Interiors*, *221*, 15–21. https://doi.org/10.1016/j.pepi.2013.06.006

Dera, P., Zhuravlev, K., Prakapenka, V., Rivers, M. L., Finkelstein, G. J., Grubor-Urosevic, O., et al. (2013). High pressure single-crystal micro X-ray diffraction analysis with GSE_ADA/RSV software. *High Pressure Research*, *33*(3), 466–484. https://doi.org/10.1080/08957959.2013.806504

Dietrich, P., & Arndt, J. (1982). Effects of pressure and temperature on the physical behaviour of mantle-relevant olivine, orthopyroxene and garnet: I. compressibility, thermal properties and macroscopic Gruneisen parameters. In W. Schreyer (Ed.), *High-Pressure Researches in Geosciences*, (pp. 293–306). Stuttgart: Schweizerbart'sche Verlagsbuchhandlunnngen.

Dolomanov, O. V., Bourhis, L. J., Gildea, R. J., Howard, J. A., & Puschmann, H. (2009). OLEX2: A complete structure solution, refinement and analysis program. *Journal of Applied Crystallography*, *42*(2), 339–341. https://doi.org/10.1107/S0021889808042726

Domeneghetti, M. C., & Steffen, G. (1992). M1, M2 site populations and distortion parameters in synthetic Mg-Fe orthopyroxenes from Mössbauer spectra and X-ray structure refinements. *Physics and Chemistry of Minerals*, *19*(5), 298–306. https://doi.org/10.1007/BF00204007

Dziewonski, A.M., & Anderson, D.L. (1981). Preliminary reference earth model. *Physics of the Earth and Planetary Interiors*, *25*(4), 297–356. https://doi.org/10.1016/0031-9201(81)90046-7

Faccenda, M., & Dal Zilio, L. (2017). The role of solid-solid phase transitions in mantle convection. *Lithos*, *268-271*, 198–224. https://doi.org/10.1016/j.lithos.2016.11.007

Fan, D., Lu, C., Xu, J., Yan, B., Yang, B., & Chen, J. (2017). Effects of water on *P-V-T* equation of state of pyrope. *Physics of the Earth and Planetary Interiors*, *267*, 9–18. http://doi.org/10.1016/j.pepi.2017.03.005

Fei, Y., Ricolleau, A., Frank, M., Mibe, K., Shen, G., & Prakapenka, V. (2007). Toward an internally consistent pressure scale. *Proceedings of the National Academy of Sciences of the United States of America*, *104*(22), 9182–9186. https://doi.org/10.1073/pnas.0609013104

Fei, Y., Saxena, S. K., & Navrotsky, A. (1990). Internally consistent thermodynamic data and equilibrium phase relations for compounds in the system MgO-SiO_2 at high pressure and high temperature. *Journal of Geophysical Research; Solid Earth*, *95*(B5), 6915–6928. https://doi.org/10.1029/JB095iB05p06915

Finkelstein, G. J., Dera, P. K., & Duffy, T. S. (2015). Phase transitions in orthopyroxene (En_{90}) to 49 GPa from single-crystal X-ray diffraction. *Physics of the Earth and Planetary Interiors*, *244*, 78–86. https://doi.org/10.1016/j.pepi.2014.10.009

Flesch, L. M., Li, B., & Liebermann, R. C. (1998). Sound velocities of polycrystalline $MgSiO_3$-orthopyroxene to 10 GPa at room temperature. *American Mineralogist*, *83*(5-6), 434–443. https://doi.org/10.2138/am-1998-5-603

Frisillo, A. L., & Barsch, G. R. (1972). Measurement of single-crystal elastic constants of bronzite as a function of pressure and temperature. *Journal of Geophysical Research (1896–1977)*, *77*(32), 6360–6384. https://doi.org/10.1029/JB077i032p06360

Frost, D. J. (2008). The upper mantle and transition zone. *Elements*, *4*(3), 171–176. https://doi.org/10.2113/GSELEMENTS.4.3.171

Ganguly, J., Freed, A. M., & Saxena, S. K. (2009). Density profiles of oceanic slabs and surrounding mantle: Integrated thermodynamic and thermal modeling, and implications for the fate of slabs at the 660 km discontinuity. *Physics of the Earth and Planetary Interiors*, *172*(3-4), 257–267. https://doi.org/10.1016/j.pepi.2008.10.005

Hogrefe, A., Rubie, D., Sharp, T., & Seifert, F. (1994). Metastability of enstatite in deep subducting lithosphere. *Nature*, *372*(6504), 351–353. https://doi.org/10.1038/372351a0

Hugh-Jones, D. (1997). Thermal expansion of $MgSiO_3$ and $FeSiO_3$ ortho-and clinopyroxenes. *American Mineralogist*, *82*(7–8), 689–696. https://doi.org/10.2138/am-1997-7-806

Hugh-Jones, D., & Angel, R. (1997). Effect of Ca^{2+} and Fe^{2+} on the equation of state of $MgSiO_3$ orthopyroxene. *Journal of Geophysical Research: Solid Earth*, *102*, L11307. 12333–12340. https://doi.org/10.1029/96JB03485

Hugh-Jones, D., Chopelas, A., & Augel, R. (1997). Tetrahedral compression in (Mg, Fe)SiO_3 orthopyroxenes. *Physics and Chemistry of Minerals*, *24*(4), 301–310. https://doi.org/10.1007/s002690050042

Hugh-Jones, D., Sharp, T., Angel, R., & Woodland, A. (1996). The transition of orthoferrosilite to high-pressure. *C2/c clinoferrosilite at ambient temperature.*, *8*(6), 1337–1346. https://doi.org/10.1127/ejm/8/6/1337

Hugh-Jones, D. A., & Angel, R. J. (1994). A compressional study of $MgSiO_3$ orthoenstatite up to 8.5 GPa. *American Mineralogist*, *79*(5–6), 405–410.

Ito, E., & Navrotsky, A. (1985). MgSiO 3 ilmenite; calorimetry, phase equilibria, and decomposition at atmospheric pressure. *American Mineralogist*, *70*(9–10), 1020–1026.

Jackson, J. M., Palko, J. W., Andrault, D., Sinogeikin, S. V., Lakshtanov, D. L., Jingyun, W., et al. (2003). Thermal expansion of natural orthoenstatite to 1473 K. *European Journal of Mineralogy*, *15*(3), 469–473. https://doi.org/10.1127/0935-1221/2003/0015-0469

Jackson, J. M., Sinogeikin, S. V., & Bass, J. D. (1999). Elasticity of $MgSiO_3$ orthoenstatite. *American Mineralogist*, *84*(4), 677–680. https://doi.org/10.2138/am-1999-0421

Jackson, J. M., Sinogeikin, S. V., & Bass, J. D. (2007). Sound velocities and single-crystal elasticity of orthoenstatite to 1073 K at ambient pressure. *Physics of the Earth and Planetary Interiors*, *161*(1–2), 1–12. https://doi.org/10.1016/j.pepi.2006.11.002

Jaffe, H., Robinson, P., & Tracy, R. (1978). Orthoferrosilite and other iron-rich pyroxenes in microperthite gneiss of the Mount Marcy area, Adirondack Mountains. *American Mineralogist*, *63*(11–12), 1116–1136.

Katsura, T., Shatskiy, A., Manthilake, M. A. G. M., Zhai, S., Yamazaki, D., Matsuzaki, T., et al. (2009). P-V-T relations of wadsleyite determined by in situ X-ray diffraction in a large-volume high-pressure apparatus. *Geophysical Research Letters*, *36*(11). https://doi.org/10.1029/2009GL038107

King, S. D., Frost, D. J., & Rubie, D. C. (2015). Why cold slabs stagnate in the transition zone. *Geology*, *43*(3), 231–234. https://doi.org/10.1130/G36320.1

Kirby, S., Stern, L., & Durham, W. (1991). Mantle phase changes and deep-earthquake faulting in subducting lithosphere. *Science*, *252*(5003), 216–225. https://doi.org/10.1126/science.252.5003.216

Kirby, S. H., Stein, S., Okal, E. A., & Rubie, D. C. (1996). Metastable mantle phase transformations and deep earthquakes in subducting oceanic lithosphere. *Reviews of Geophysics*, *34*(2), 261–306. https://doi.org/10.1029/96RG01050

Koch-Müller, M., Matsyuk, S. S., & Wirth, R. (2004). Hydroxyl in omphacites and omphacitic clinopyroxenes of upper mantle to lower crustal origin beneath the Siberian platform. *American Mineralogist*, *89*(7), 921–931. https://doi.org/10.2138/am-2004-0701

Kung, J., Li, B., Uchida, T., Wang, Y., Neuville, D., & Liebermann, R. C. (2004). In situ measurements of sound velocities and densities across the orthopyroxene-high-pressure clinopyroxene transition in $MgSiO_3$ at high pressure. *Physics of the Earth and Planetary Interiors*, *147*(1), 27–44. https://doi.org/10.1016/j.pepi.2004.05.008

Li, B., Kung, J., Liu, W., & Liebermann, R. C. (2014). Phase transition and elasticity of enstatite under pressure from experiments and first-principles studies. *Physics of the Earth and Planetary Interiors*, *228*, 63–74. https://doi.org/10.1016/j.pepi.2013.11.009

Lin, C.-C. (2004). Pressure-induced polymorphism in enstatite ($MgSiO_3$) at room temperature: Clinoenstatite and orthoenstatite. *Journal of Physics and Chemistry of Solids*, *65*(5), 913–921. https://doi.org/10.1016/j.jpcs.2003.09.028

Liu, J., Zhang, J., Flesch, L., Li, B., Weidner, D. J., & Liebermann, R. C. (1999). Thermal equation of state of stishovite. *Physics of the Earth and Planetary Interiors*, *112*(3-4), 257–266. https://doi.org/10.1016/S0031-9201(99)00037-0

Momma, K., & Izumi, F. (2011). VESTA 3 for three-dimensional visualization of crystal, volumetric and morphology data. *Journal of Applied Crystallography*, *44*(6), 1272–1276. https://doi.org/10.1107/S0021889811038970

Nestola, F., Ballaran, T. B., Balic-Zunic, T., Secco, L., & Dal Negro, A. (2008). The high-pressure behavior of an Al- and Fe-rich natural orthopyroxene. *American Mineralogist*, *93*(4), 644–652. https://doi.org/10.2138/am.2008.2693

Nishi, M., Kubo, T., Ohfuji, H., Kato, T., Nishihara, Y., & Irifune, T. (2013). Slow Si-Al interdiffusion in garnet and stagnation of subducting slabs. *Earth and Planetary Science Letters*, *361*, 44–49. https://doi.org/10.1016/j.epsl.2012.11.022

Nishihara, Y., Takahashi, E., Matsukage, K. N., Iguchi, T., Nakayama, K., & Funakoshi, K.-i. (2004). Thermal equation of state of $(Mg_{0.91}Fe_{0.09})_2SiO_4$ ringwoodite. *Physics of the Earth and Planetary Interiors*, *143-144*, 33–46. https://doi.org/10.1016/j.pepi.2003.02.001

Ohi, S., & Miyake, A. (2016). Phase transitions between high-and low-temperature orthopyroxene in the $Mg_2Si_2O_6$-$Fe_2Si_2O_6$ system. *American Mineralogist*, *101*(6), 1414–1422. https://doi.org/10.2138/am-2016-5394

Ono, S., Kikegawa, T., & Higo, Y. (2018). Decomposition boundary from high-pressure clinoenstatite to wadsleyite + stishovite in MgSiO3. *American Mineralogist*, *103*(9), 1512–1515. https://doi.org/10.2138/am-2018-6313CCBY

Periotto, B., Balić-Žunić, T., Nestola, F., Katerinopoulou, A., & Angel, R. J. (2012). Re-investigation of the crystal structure of enstatite under high-pressure conditions. *American Mineralogist*, *97*(10), 1741–1748. https://doi.org/10.2138/am.2012.4157

Rauch, M., & Keppler, H. (2002). Water solubility in orthopyroxene. *Contributions to Mineralogy and Petrology*, *143*(5), 525–536. https://doi.org/10.1007/s00410-002-0365-6

Rivers, M., Prakapenka, V. B., Kubo, A., Pullins, C., Holl, C. M., & Jacobsen, S. D. (2008). The COMPRES/GSECARS gas-loading system for diamond anvil cells at the advanced photon source. *High Pressure Research*, *28*(3), 273–292. https://doi.org/10.1080/08957950802333593

Sarver, J., & Hummel, F. (1962). Stability relations of magnesium metasilicate polymorphs. *Journal of the American Ceramic Society*, *45*(4), 152–156. https://doi.org/10.1111/j.1151-2916.1962.tb11110.x

Serghiou, G., Boehler, R., & Chopelas, A. (2000). Reversible coordination changes in crystalline silicates at high pressure and ambient temperature. *Journal of Physics: Condensed Matter*, *12*(6), 849–857. https://doi.org/10.1088/0953-8984/12/6/309

Sheldrick, G. M. (2008). A short history of SHELX. *Acta Crystallographica. Section A*, *64*(1), 112–122. https://doi.org/10.1107/S0108767307043930

Shinmei, T., Tomioka, N., Fujino, K., Kuroda, K., & Irifune, T. (1999). In situ X-ray diffraction study of enstatite up to 12 GPa and 1473 K and equations of state. *American Mineralogist*, *84*(10), 1588–1594. https://doi.org/10.2138/am-1999-1012

Skinner, B. J. (1966). Thermal expansion. In S. P. Clark, Jr. (Ed.), *Handbook of physical constants*, (pp. 75–95). Boulder, Colorado: Geological Society of America. https://doi.org/10.1130/MEM97-p75

Stachel, T., & Harris, J. W. (2008). The origin of cratonic diamonds — Constraints from mineral inclusions. *Ore Geology Reviews*, *34*(1-2), 5–32. https://doi.org/10.1016/j.oregeorev.2007.05.002

Stalder, R., Karimova, A., & Konzett, J. (2015). OH-defects in multiple-doped orthoenstatite at 4–8 GPa: Filling the gap between pure and natural systems. *Contributions to Mineralogy and Petrology*, *169*(4), 1–10.

Sueno, S., Cameron, M., & Prewitt, C. (1976). Orthoferrosilite: High-temperature crystal chemistry. *American Mineralogist*, *61*(1–2), 38–53.

Syracuse, E. M., van Keken, P. E., & Abers, G. A. (2010). The global range of subduction zone thermal models. *Physics of the Earth and Planetary Interiors*, *183*(1-2), 73–90. https://doi.org/10.1016/j.pepi.2010.02.004

Tarantino, S. C., Domeneghetti, M. C., Carpenter, M. A., Shaw, C. J., & Tazzoli, V. (2002). Mixing properties of the enstatite-ferrosilite solid solution: I. A macroscopic perspective. *European Journal of Mineralogy*, *14*(3), 525–536. https://doi.org/10.1127/0935-1221/2002/0014-0525

Van Mierlo, W., Langenhorst, F., Frost, D., & Rubie, D. (2013). Stagnation of subducting slabs in the transition zone due to slow diffusion in majoritic garnet. *Nature Geoscience*, *6*(5), 400–403. https://doi.org/10.1038/ngeo1772

Walter, M., Kohn, S., Araujo, D., Bulanova, G., Smith, C., Gaillou, E., et al. (2011). Deep mantle cycling of oceanic crust: Evidence from diamonds and their mineral inclusions. *Science*, *334*(6052), 54–57. https://doi.org/10.1126/science.1209300

Wang, Y., Uchida, T., Zhang, J., Rivers, M. L., & Sutton, S. R. (2004). Thermal equation of state of akimotoite $MgSiO_3$ and effects of the akimotoite–garnet transformation on seismic structure near the 660 km discontinuity. *Physics of the Earth and Planetary Interiors*, *143-144*, 57–80. https://doi.org/10.1016/j.pepi.2003.08.007

Weidner, D. J., Wang, H., & Ito, J. (1978). Elasticity of orthoenstatite. *Physics of the Earth and Planetary Interiors*, *17*(2), P7–P13. https://doi.org/10.1016/0031-9201(78)90043-2

Woodland, A. B. (1998). The orthorhombic to high-*P* monoclinic phase transition in Mg-Fe pyroxenes: Can it produce a seismic discontinuity? *Geophysical Research Letters*, *25*(8), 1241–1244. https://doi.org/10.1029/98GL00857

Xu, J., Zhang, D., Dera, P., Zhang, B., & Fan, D. (2017). Experimental evidence for the survival of augite to transition zone depths, and implications for subduction zone dynamics. *American Mineralogist*, *102*(7), 1516–1524. https://doi.org/10.2138/am-2017-5959

Xu, J., Zhang, D., Fan, D., Dera, P. K., Shi, F., & Zhou, W. (2019). Thermoelastic properties of eclogitic garnets and omphacites: Implications for deep subduction of oceanic crust and density anomalies in the upper mantle. *Geophysical Research Letters*, *46*, 179–188. https://doi.org/10.1029/2018GL081170

Xu, J., Zhang, D., Fan, D., Zhang, J. S., Hu, Y., Guo, X., et al. (2018). Phase transitions in orthoenstatite and subduction zone dynamics: Effects of water and transition metal ions. *Journal of Geophysical Research: Solid Earth*, *123*, 2723–2737. https://doi.org/10.1002/2017JB015169

Xu, W.-L., Zhou, Q.-J., Pei, F.-P., Yang, D.-B., Gao, S., Li, Q.-L., & Yang, Y. H. (2013). Destruction of the North China Craton: Delamination or thermal/chemical erosion? Mineral chemistry and oxygen isotope insights from websterite xenoliths. *Gondwana Research*, *23*(1), 119–129. https://doi.org/10.1016/j.gr.2012.02.008

Xu, Z., Ma, M., Li, B., Hong, X., Han, L., & Zhou, X. (2016). The elasticity of natural hypersthene and the effect of Fe and Al substitution. *High Pressure Research*, *36*(1), 63–72. https://doi.org/10.1080/08957959.2015.1136623

Yang, H., & Ghose, S. (1994). Thermal expansion, Debye temperature and Grüneisen parameter of synthetic (Fe, Mg)SiO_3 orthopyroxenes. *Physics and Chemistry of Minerals*, *20*(8), 575–586. https://doi.org/10.1007/BF00211853

Ye, Y. (2016). Hydration effects on crystal structures and equations of state for silicate minerals in the subducting slabs and mantle transition zone. *Science China Earth Sciences*, *59*(4), 707–719. https://doi.org/10.1007/s11430-015-5260-x

Zhang, D., Dera, P. K., Eng, P. J., Stubbs, J. E., Zhang, J. S., Prakapenka, V. B., et al. (2017). High pressure single crystal diffraction at PX^2. *Journal of visualized experiments: JoVE*, *119*, e54660. https://www.jove.com/video/54660

Zhang, D., Jackson, J. M., Chen, B., Sturhahn, W., Zhao, J., Yan, J., & Caracas, R. (2013). Elasticity and lattice dynamics of enstatite at high pressure. *Journal of Geophysical Research: Solid Earth*, *118*, 4071–4082. https://doi.org/10.1002/jgrb.50303

Zhang, D., Jackson, J. M., Sturhahn, W., & Xiao, Y. (2011). Local structure variations observed in orthoenstatite at high pressures. *American Mineralogist*, *96*(10), 1585–1592. https://doi.org/10.2138/am.2011.3721

Zhang, J. S., & Bass, J. D. (2016). Single crystal elasticity of natural Fe-bearing orthoenstatite across a high-pressure phase transition. *Geophysical Research Letters*, *43*, 8473–8481. https://doi.org/10.1002/2016GL069963

Zhang, J. S., Dera, P., & Bass, J. D. (2012). A new high-pressure phase transition in natural Fe-bearing orthoenstatite. *American Mineralogist*, *97*(7), 1070–1074. https://doi.org/10.2138/am.2012.4072

Zhang, J. S., Reynard, B., Montagnac, G., & Bass, J. D. (2014). Pressure-induced *Pbca-P*$2_1/c$ phase transition of natural orthoenstatite: The effect of high temperature and its geophysical implications. *Physics of the Earth and Planetary Interiors*, *228*, 150–159. https://doi.org/10.1016/j.pepi.2013.09.008

Zhang, J. S., Reynard, B., Montagnac, G., Wang, R. C., & Bass, J. D. (2013). Pressure-induced *Pbca-P*$2_1/c$ phase transition of natural orthoenstatite: Compositional effect and its geophysical implications. *American Mineralogist*, *98*(5–6), 986–992. https://doi.org/10.2138/am.2013.4345

Zhao, Y., Schiferl, D., & Shankland, T. J. (1995). A high PT single-crystal X-ray diffraction study of thermoelasticity of $MgSiO_3$ orthoenstatite. *Physics and Chemistry of Minerals*, *22*(6), 393–398. https://doi.org/10.1007/BF00213337